Ultra-long period and small-amplitude tsunami generated following the July 2020 Alaska M$_w$7.8 tsunamigenic earthquake

Mohammad Heidarzadeh [a,*], Iyan E. Mulia [b]

[a] *Department of Civil & Environmental Engineering, Brunel University London, Uxbridge, UB8 3PH, UK*
[b] *Prediction Science Laboratory, RIKEN Cluster for Pioneering Research, Kobe, Japan*

ABSTRACT

The July 2020 M$_w$7.8 Alaska tsunamigenic earthquake was a fresh call for potential large tsunamis associated with the Aleutian subduction zone. The second largest ever-recorded earthquake worldwide (M$_w$ 9.2) occurred in this zone in 1964 indicating its massive earthquake and tsunami risk. Our analysis of the July 2020 tsunami revealed that it involves very long period waves (51–64 min) which is unusual for an M$_w$7.8 earthquake. The tsunami coastal amplitude was small (~0.5 m) which is much smaller than that usually expected from a tsunamigenic earthquake of this size. Here, through numerical simulations and spectral analyses, we explain the ultra-long period and small amplitude waves of the tsunami. Our analysis using an analytical equation showed that the ultra-long period of the tsunami (51–64 min) can be reproduced using the shallow water depth around the source region (100–200 m) and the length of the coseismic deformation area (~100 km). By comparing the coastal amplitude of this event with four other similar-size and similar-mechanism earthquakes (thrust M$_w$7.8), we attribute the relatively small coastal amplitude of this tsunami to the deep focal depth of the earthquake (28 km) and the extremely shallow water around the source region.

1. Introduction

Offshore Alaska was the site of a large M$_w$7.8 earthquake on July 22, 2020 which was followed by a small tsunami with a coastal runup of around half a meter (Fig. 1). The United States Geological Survey (USGS) located the earthquake at 158.554°W and 55.068°N at the depth of 28.0 km with an origin time of 06:12:44 (UTC). The earthquake was of dominant thrust mechanism with USGS focal parameters of strike angle: 232°, dip angle: 20° and rake angle: 73°. According to media reports, this offshore earthquake did not make significant damage although the shaking was felt across most of the Alaska Peninsula. A tsunami warning was issued by the US Tsunami Warning System (https://www.tsunami.gov/) following the earthquake; however, the warning was called off after confirming that the tsunami height was minimal based on the tsunami records on offshore Deep-ocean Assessment and Reporting of Tsunamis (DART) devices. The DART systems recorded maximum zero-to-crest amplitudes of less than 1 cm while the nearby coastal tide gauges registered tsunami amplitude of less than 30 cm (Fig. 2).

The July 2020 M$_w$7.8 tsunamigenic earthquake was generated in the Aleutian subduction zone where the Pacific Plate is subducting beneath the North American Plate at the rate of 5.5–6.0 cm/yr (Li et al., 2016). The Aleutian subduction zone was responsible for the second largest instrumentally-recorded earthquake worldwide: the March 1964 M$_w$9.2 Alaska earthquake (Plafker et al., 1969) (Fig. 1). Based on the USGS earthquake catalogue, at least 16 M ≥ 7.8 earthquakes were recorded in this zone since 1900, among which the two most notable events are the 1946 (M$_w$8.6) and 1964 (M$_w$9.2) events (Fig. 1, orange circles). The 1946 Aleutian tsunami produced 42 m runup and caused five deaths in the near-field, combined with a runup of 16 m and 159 deaths in the far-field, i.e. Hawaii (Lopez and Okal,. 2006; Okal et al., 2002; Johnson and Satake, 1997). The 1964 Alaska tsunami has been reported to have killed 130 people (Clague et al., 1994) and caused extensive damage. Numerous submarine landslides were reported following the 1964 Alaska earthquake which further intensified the damaging impacts of the event by triggering local landslide tsunamis (Haeussler et al., 2014).

The objective of this research is to understand the sea level characteristics of the July 2020 Alaska tsunami. In particular, there are two unusual signatures in the sea level data of the 2020 tsunami, which motivated this research: (i) the tsunami has a very long period of ~60 min (Fig. 2) which is unusual for a tsunami from an M$_w$7.8 earthquake;
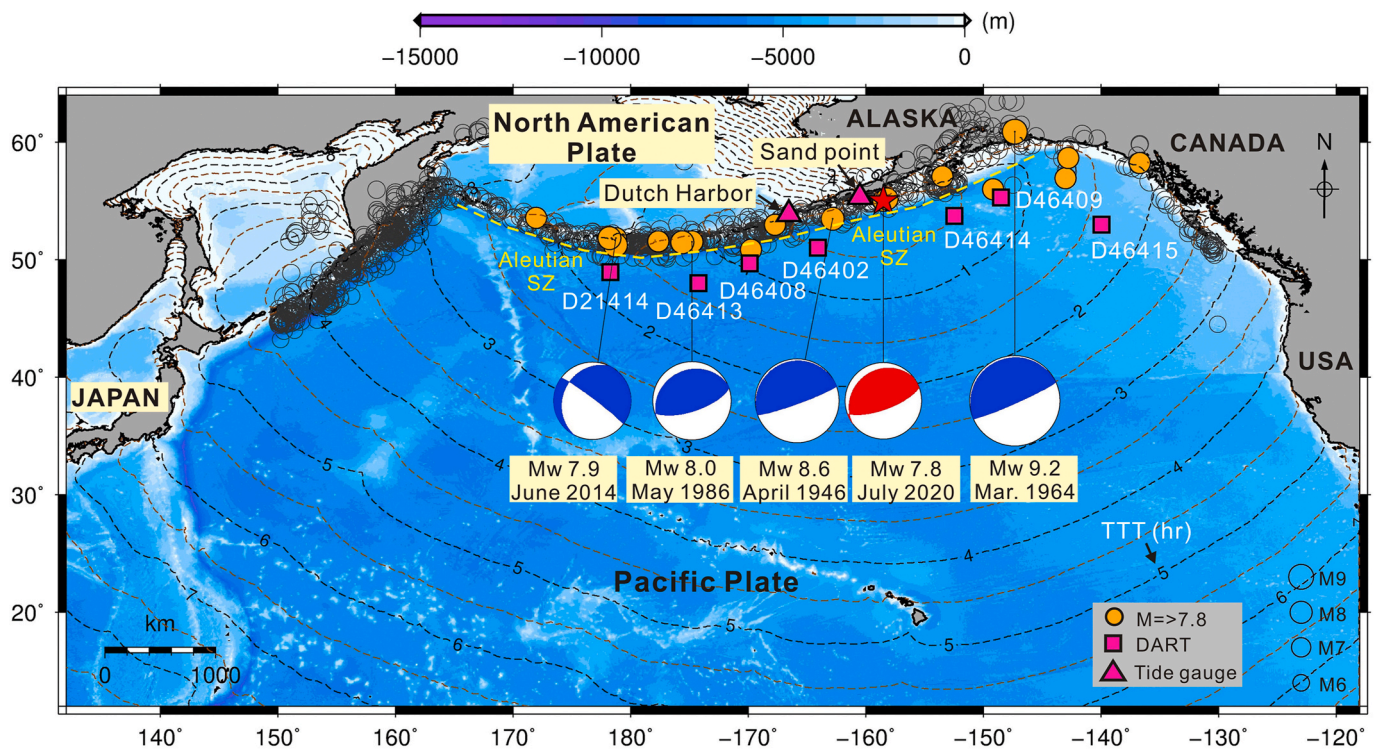

Fig. 1. The epicenter (red star) and mechanism of the July 22, 2020 Alaska (USA) earthquake and tsunami. Orange circles represent M ≥ 7.8 earthquakes since 1900 whereas open circles show all M > 6 earthquakes since 1900. The earthquake epicenter and mechanism information are based on the USGS earthquake catalogue except for the focal mechanisms of the 1946 and 1964 earthquakes which are from Johnson and Satake (1997) and Stauder and Bollinger (1966), respectively. Dashed contours give tsunami travel times (TTT) in hours with 0.5 h intervals which are calculated using the TTT program by Geoware, (2011). SZ stands for subduction zone. Names starting with "D" stand for DART stations. (For interpretation of the references to color in this figure legend, the reader is referred to the Web version of this article.)

(ii) the tsunami's coastal amplitude is significantly smaller than those normally generated by an M_w7.8 offshore earthquake. For comparison, a similar-magnitude (M_w7.8) and similar-mechanism (thrust) earthquake at the depth of 15.1 km in Kaikoura, New Zealand generated a tsunami with period of 15–20 min and coastal runup of up to 7 m (Power et al., 2017; Heidarzadeh et al., 2019). We note that the focal depth of the Kaikoura event (15.1 km) was shallower than that of the Alaska event (28.0 km). Here, we apply sea level data analysis and numerical modeling of tsunami propagation to study the 2020 Alaska tsunami and to explain the above two unusual characteristics of the tsunami. The innovation of this study is that, for the first time, we apply analytical equations and numerical simulations to explain the unusual tsunami waves generated by an M_w7.8 earthquake.

2. Data and methods

Our data comprises sea level records of the tsunami, ocean bathymetry and the earthquake fault parameters. Sea level records are from tide gauge stations in Sand Point and Dutch Harbor as well as seven DARTs (Fig. 2). The sampling interval for all sea level data is 1 min. Both tide gauge and DART records belong to the National Ocean Service of the US National Oceanic and Atmospheric Administration (NOAA). The initial part of the DART data includes under-sampled seismic waves which are called here as seismic noise (Fig. 2); although they are not useful for tsunami characterization, An et al. (2017) demonstrated that they can be helpful for estimating earthquake parameters. The least-squares method of Grinsted (2008) was employed to estimate the tidal signals and to remove them from the original sea level records. The bathymetry data comes from the General Bathymetric Charts of the Oceans (GEBCO) 2020 digital grid atlas (IOC et al., 2003; Weatherall et al., 2015) which has a spatial resolution of 15 arc-sec. The fault

parameters of the July 2020 Alaska earthquake is provided by the USGS (https://earthquake.usgs.gov/earthquakes/eventpage/us7000asvb/finite-fault) which is in the form of a finite fault model with 345 subfaults of size 10 km × 10 km. The strike and dip angles of the subfaults were fixed at 232° and 20°, respectively, their depths were varied in the range of 6.1–54.0 km and the slip on the subfaults was up to 3.7 m. The USGS source model is obtained through inversion of worldwide seismic observations of the earthquake. Here, we applied a trial-and-error approach to adjust the length, width and slip of the USGS model in order to reproduce tsunami observations.

Our method is a combination of sea level data analysis and numerical modeling. Fourier transform and Wavelet (frequency-time) analyses were performed on the sea level data. For Fourier transform, the Welch algorithm (Welch, 1967; Mathworks, 2020) was applied considering half-window overlaps and Hanning windows (Heidarzadeh et al., 2017a). The Fourier analysis was conducted for both tsunami and the background signal (i.e. part of the waveform before tsunami arrival at each sea level station) in order to identify main tsunami energy channels. The lengths of the tsunami and background waveforms used for spectral analyses, were 150–200 min and 120–150 min, respectively. For Wavelet analysis, we used the Wavelet package of Torrence and Compo, (1998) considering the Morlet mother function with a wave-number of 6 and a scale width of 0.10 (Heidarzadeh et al., 2020).

We employed a well-validated tsunami simulation package called JAGURS (Baba et al., 2015) to simulate tsunami propagation and coastal amplification. We solved Shallow Water Equations on a three-level nested grid system with grid sizes of 180 arc-sec, 60 arc-sec, and 20 arc-sec from the largest domain (far from the coast) to the smallest domain (around the coast), respectively (Fig. 5a). Among a few numerical packages available for tsunami modeling, JAGURS is favored due to its nesting grid capability and its flexibility for both serial and
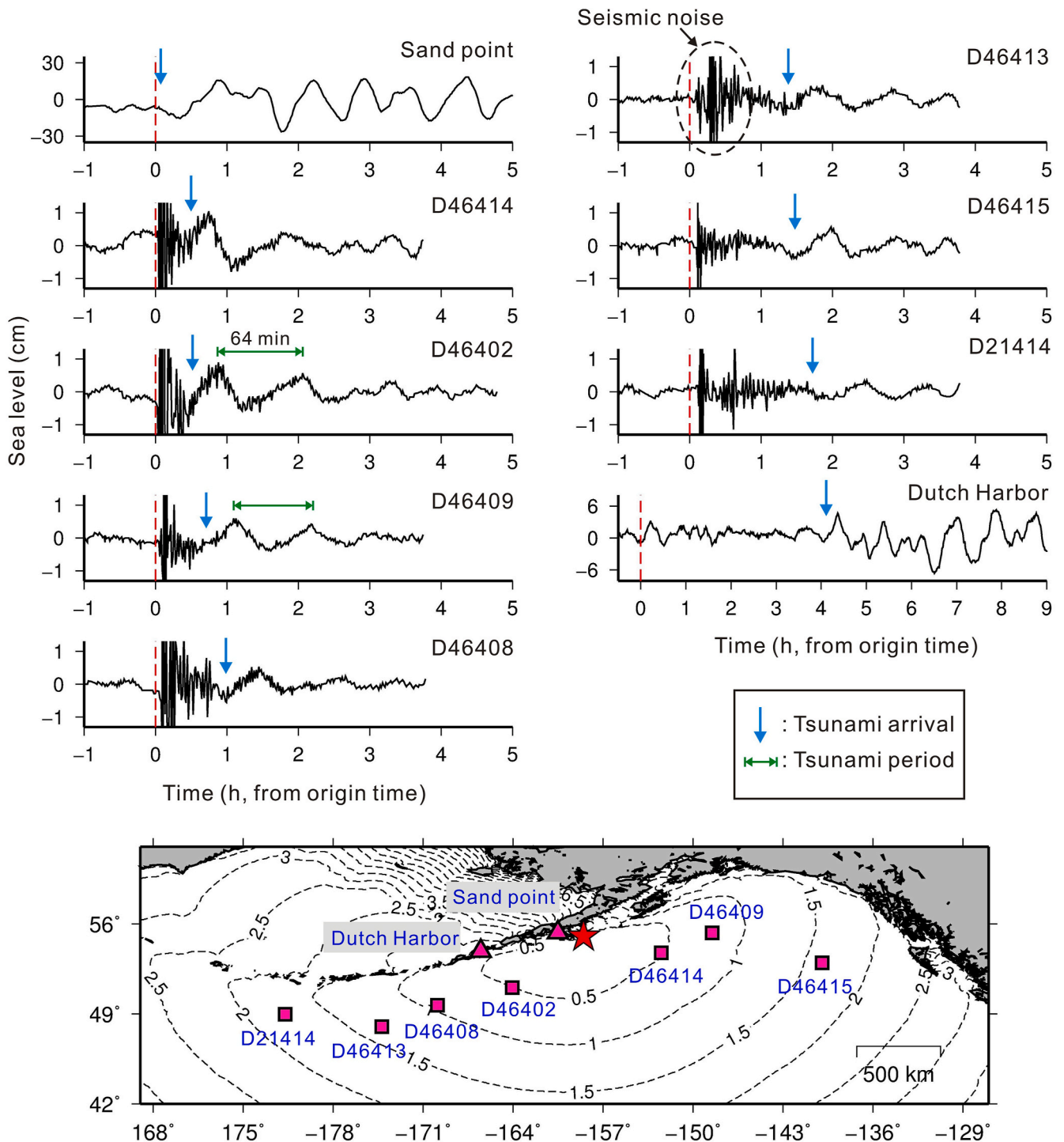
Fig. 2. Sea level waveforms of the July 22, 2020 Alaska (USA) tsunami recorded on two tide gauges (Sand Point, and Dutch harbor) and seven DARTs.

parallel computations. We run the tsunami for a total simulation time of 9 h with time step of 1.0 s to satisfy the stability condition of the numerical scheme (Courant et al., 1928; Heidarzadeh et al., 2009). To calculate coseismic crustal deformation due to the earthquake, the analytical dislocation modeling approach of Okada (1985) was applied. An instantaneous coseismic deformation is assumed which implies that the initial sea surface displacement is the same as the crustal deformation. This is the common practice for modeling tsunamis generated by earthquakes because the speed of tsunami wave propagation is approximately hundred times lower than the speed of seismic waves (e. g., Satake, 1987).

3. Tsunami waveforms and spectral analysis

Deep-ocean and coastal records of the Alaska tsunami measured on DARTs and tide gauges, respectively, are shown in Fig. 2 and their characteristics are listed in Table 1. The deep-ocean zero-to-crest amplitudes are 0.3–1.0 cm with an average of 0.6 cm whereas the coastal amplitudes are 5.7–24.0 cm averaging 14.9 cm (Table 1). The tsunami amplitudes decay rapidly on DARTs while large-amplitude waves persist for at least 5 h on two coastal records in Sand Point and Dutch Harbor (Fig. 2). Longer duration of tsunami waves on coastal tide gauges is attributed to various coastal and shelf features such as reflections,
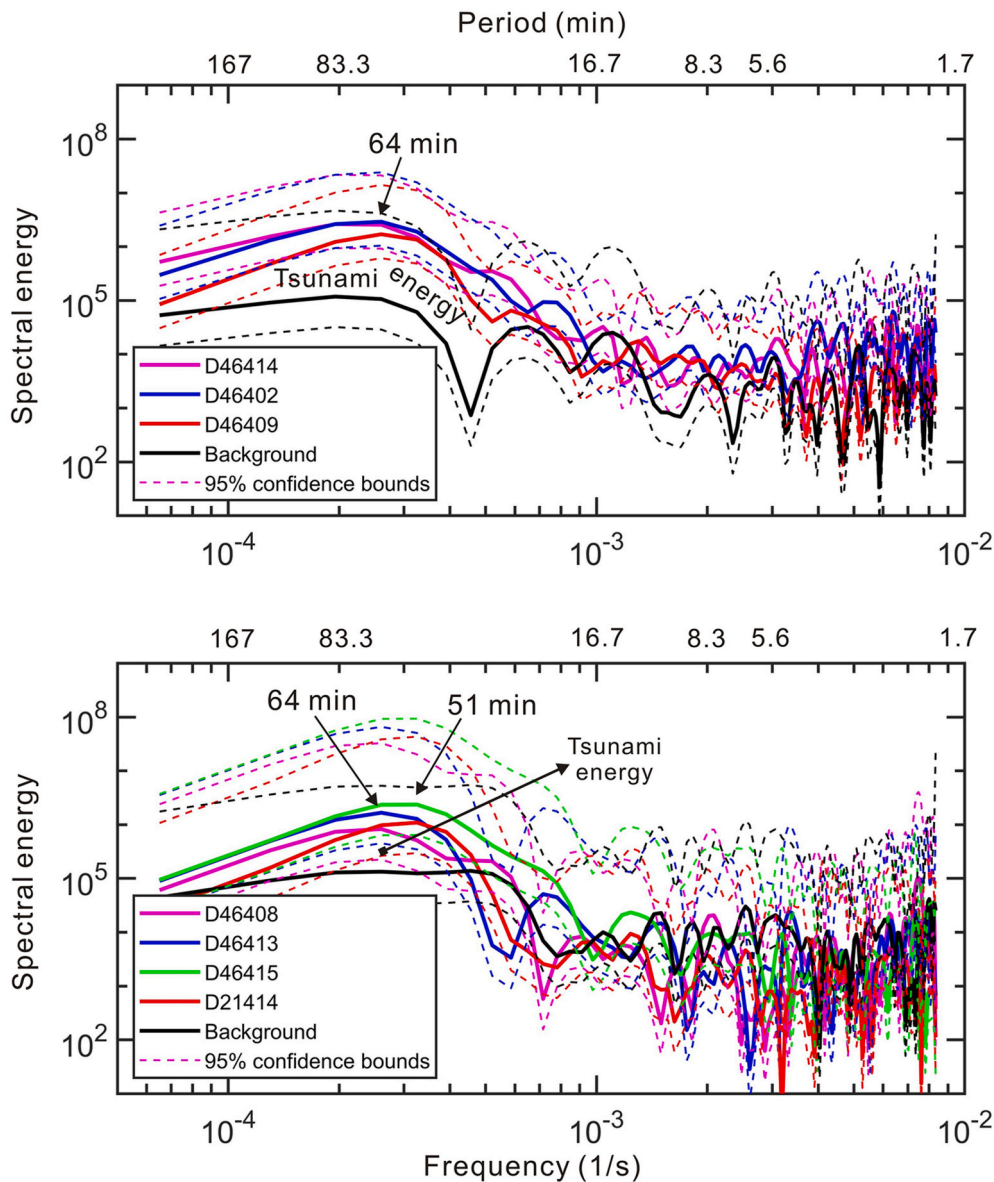
Fig. 3. Spectra of the DART tsunami waveforms of the July 22, 2020 Alaska (USA) tsunami based on Fourier analysis.

resonance of the wave inside harbors as well as trapped edge waves (e.g. Saito et al., 2014; Heidarzadeh; Satake, 2014; Satake et al., 2020).

Fourier analysis (Fig. 3; color spectra) and comparison with background spectra (Fig. 3; black spectra) revealed that the dominant tsunami period is 51–64 min. It is noted that the tsunami dominant period is influenced by the azimuthal angle of the DART station from the epicenter. We performed Fourier analysis only for DART records because they are mostly free from various coastal and shelf features, and thus carry mainly tsunami source features (e.g. Rabinovich, 1997). Wavelet plots demonstrate the temporal changes of the tsunami dominant periods at three DARTs (Fig. 4). It can be seen that the dominant periods of 51–64 min are the main signal available in the DART waveforms. We note that the strong signal at the period of 2–7 min in the Wavelet plots belong to the under-sampled seismic noise of the earthquake recorded on the DARTs and thus they do not represent the tsunami. The short duration (~2 h) of the energetic tsunami waves on DARTs is also confirmed on Wavelet plots (Fig. 4).

4. Numerical simulations and validation

The purpose of numerical modeling was to confirm the coseismic tsunami source of the July 2020 event and to validate it through DART and tide gauge observation. We use the validated source model for further analyses in the next sections. The results of tsunami simulation using the USGS source model is shown in Fig. 5d (blue waveforms) indicating that the simulated waveforms arrive 10–20 min earlier than the observations in some stations. Therefore, it is necessary to further adjust the tsunami source. The main reason for lack of a perfect match between simulations and observation is that the USGS source model is obtained through the inversion of only seismic observations of the earthquake. Therefore, it is natural that such a model does not give a perfect match for tsunami observations although it yields better results for seismic waveforms (e.g. Yokota et al., 2011; Satake and Heidarzadeh, 2017). It has been noted by several authors that a more accurate tsunami source can be achieved by a joint seismic-tsunami inversion (e.g., Gusman et al., 2015).

Inspired by the USGS source model, we considered a rectangular source model with uniform slip to achieve a better match between
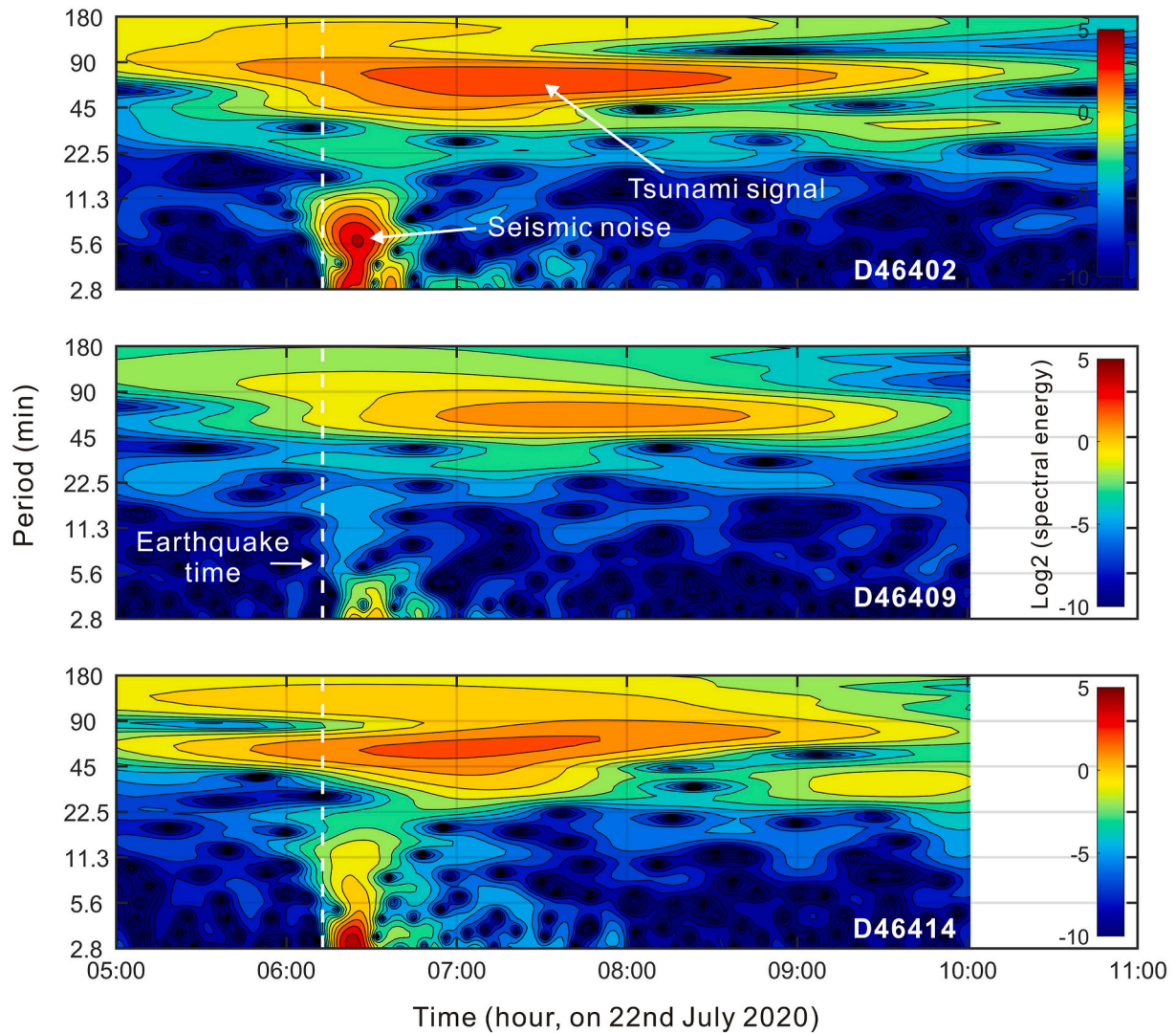
Fig. 4. Wavelet analysis for three DART tsunami waveforms of the July 22, 2020 Alaska (USA) tsunami. The white dashed line shows the origin time of the earthquake.

observations and simulations through a trial-and-error approach. First, the fault length and width are assumed as 110 km and 70 km, respectively. Then, the uniform slip of 1.7 m is calculated based on a depth-dependent earth rigidity of 4.3×10^{10} N/m^2 proposed by Sallarès and Ranero (2019). Similar scaling laws are proposed by An et al. (2018). Other fault parameters such as strike angle (232°), dip angle (20°), rake angle (73°), and depth (28 km) are taken from the USGS model. This model is called as "uniform fault" here. In fact, our uniform fault is a simplified, but improved, version of the USGS fault model which is improved through tsunami observations. The coseismic crustal deformation due to the USGS and our uniform-fault models are given in Fig. 5b and c, respectively.

The tsunami simulations using our uniform fault model produces good agreement between observation and simulation waveforms (Fig. 5d, red waveforms). The simulated waves using the USGS model (Fig. 5d, blue waveforms) arrive earlier and have shorter wave periods whereas those using our uniform fault model match the observation well. Snapshots of tsunami propagation (Fig. 6a) reveal that tsunami arrives in west Canada, Hawaii and west US within 2–5 h. Plot of maximum tsunami amplitudes during the entire tsunami simulations (Fig. 6b) indicates that most of the far-field tsunami amplitudes are directed towards west Canada and west USA. It is long known that tsunami energy travels along normal direction to the fault orientation in

the far field (Ben-Menahem and Rosenman, 1972; Okal, 1988; Synolakis and Bernard, 2006). Given the strike angle of 232° for the 2020 Alaska earthquake (direction NE-SW; Fig. 5b and c), the normal direction to the strike angle is 142° which is direction NW-SE, towards west Canada and west USA.

5. The ultra-long period waves of the 2020 Alaska tsunami

The tsunami waveforms and spectra of the July 2020 Alaska event (M_w7.8) are compared with those of the March 2011 Japan event (M_w9.0) at three DART stations (Fig. 7). Despite the much smaller magnitude of the Alaska event compared to the 2011 Japan earthquake, the dominant period of the 2020 Alaska tsunami (51–64 min) is much longer than the dominant period of the 2011 Japan event (20–26 min). Traditionally, it has been thought that the larger the magnitude of the earthquake, the longer its tsunami period would be. However, this is not the case for the 2020 Alaska tsunami. We attribute the ultra-long period of the 2020 Alaska tsunami to the rather shallow water depth of the source region (depth = 100–200 m; Fig. 8b). The dominant period of a tsunami (T) can be approximated using the length of the main coseismic crustal deformation (L) and the water depth (d) at the epicentral area applying the following equation (Heidarzadeh and Satake, 2015):
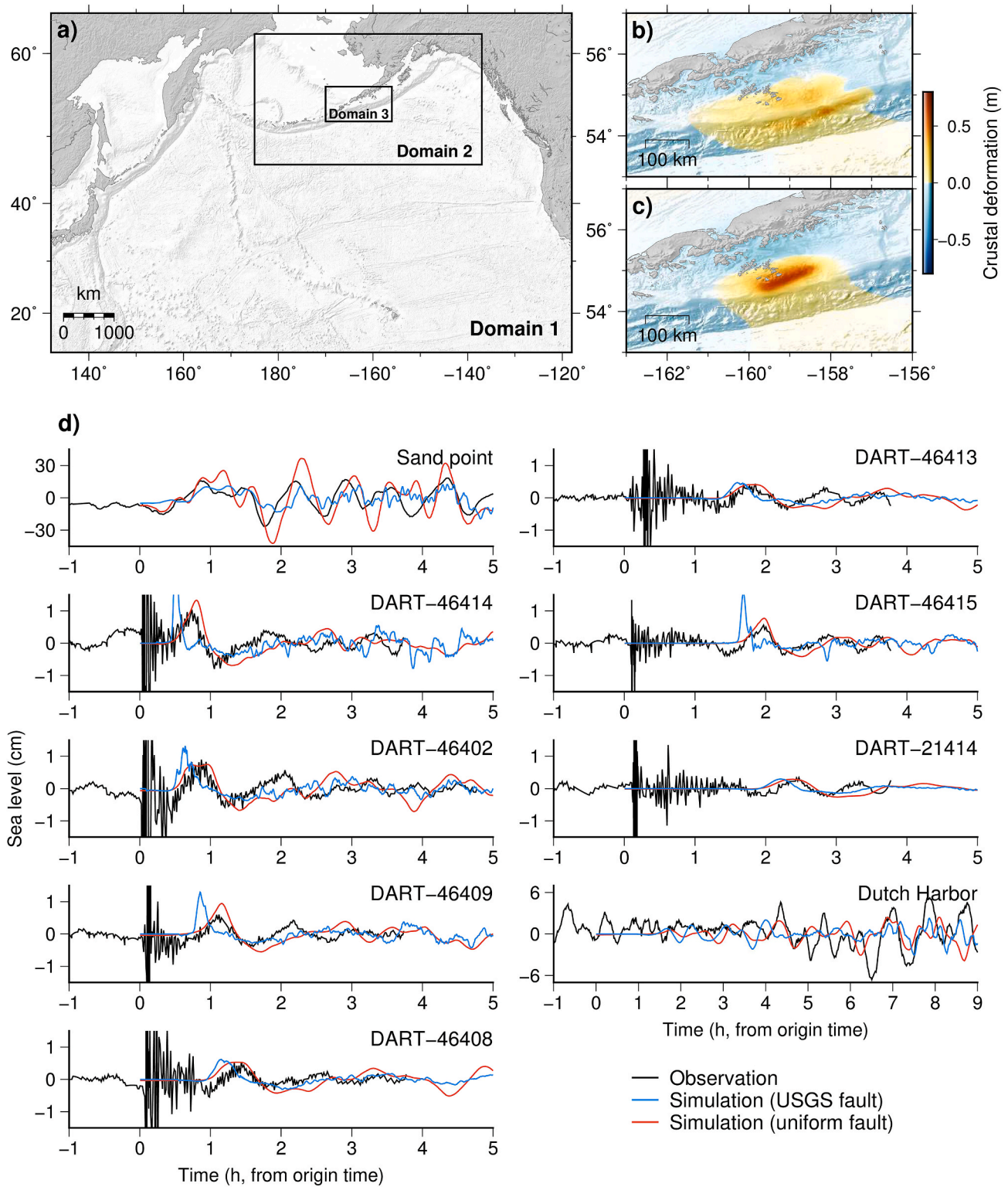
Fig. 5. a. Computational domain comprising of three levels of nested grids with spatial resolutions of 180 arc-sec (Domain-1), 60 arc-sec (Domain-2) and 20 arc-sec (Domain-3). **b.** Crustal deformation obtained from the USGS finite fault. **c.** Crustal deformation calculated using our uniform-fault model. **d.** Comparison of observed (black) and simulated (blue for the USGS fault and red for our uniform-fault) waveforms for the July 2020 Alaska (USA) tsunami. (For interpretation of the references to color in this figure legend, the reader is referred to the Web version of this article.)

$$T = 2L \left/ \sqrt{gd} \right. \tag{1}$$

where *g* is gravitational acceleration (9.81 m/s^2). We note that tsunami energy usually occurs over a period band rather than a single period

because of the heterogeneous shape and non-instantaneous occurrence of coseismic crustal deformation. Equation (1) gives the dominant tsunami period using the length of the largest deformation area, rather than the whole period band.

For the 2020 Alaska tsunami, the length of the crustal deformation is

Table 1
Characteristics of the sea level waveforms of the July 22, 2020 Alaska (USA) tsunami.

Station name	Type	Longitude (°E/°W)	Latitude (°N)	Max. amplitude[a] (cm)	Max. wave height[b] (cm)	Dominant period (min)
Sand point	Tide gauge	−160.502	55.337	24.0	41.0	N/A[c]
Dutch harbor	Tide gauge	−166.533	53.883	5.7	10.4	N/A[c]
D46414	DART	−152.483	53.726	1.0	1.8	64
D46402	DART	−163.948	50.978	0.9	1.5	64
D46409	DART	−148.550	55.310	0.6	0.9	64
D46408	DART	−169.900	49.662	0.5	0.8	64
D46413	DART	−174.228	48.000	0.4	0.8	64
D46415	DART	−139.950	52.980	0.6	0.9	51
D21414	DART	178.227	48.968	0.3	0.6	51

[a] Zero-to-crest amplitude.

[b] Trough-to-crest height.

[c] Not Applicable.

80–100 km at the water depth of 100–200 m based on our validated source model (Figs. 5c and 8b). For the 2011 Japan tsunami, the respective values are 80–120 km and 3000–6000 m (Fig. 8a). While the total length of the 2011 event's crustal deformation is > 200 km, we consider only the length of the largest deformation area as we mainly concern about the dominant tsunami period in this study. Using such input parameters, Equation (1) results in dominant period of 17–20 min for the 2011 Japan event (Figs. 8c) and 60–75 min for the 2020 Alaska tsunami (Fig. 8d). These values are consistent with real tsunami dominant periods obtained through Fourier analysis of tsunami observations for the two events (Fig. 7b). Therefore, our analytical study applying Equation (1) explains that the ultra-long period of the 2020 Alaska tsunami is attributed to the generation of the tsunami in extreme shallow water depth of 100–200 m of the continental shelf.

6. The small coastal amplitude of the July 2020 Alaska tsunami

The coastal amplitudes of the 2020 Alaska tsunami were much smaller than other tsunamis generated by similar-magnitude and similar-mechanism earthquakes. For comparison, the 2016 Kaikoura (New Zealand) and 2012 Haida Gwaii (Canada) tsunamis were both generated by M_w7.8 thrust earthquakes which generated maximum coastal runup of 6 m (Power et al., 2017; Heidarzadeh et al., 2019) and 13 m (Gusman et al., 2016), respectively. We note that the 2020 Alaska earthquake occurred at the depth of 28 km while the depths of the 2016 Kaikoura and 2012 Haida Gwaii events were 15 km and 14 km, respectively.

In general, several factors may influence coastal amplitude of a tsunami including: amplitude of coseismic crustal deformation at the tsunami source (or magnitude of the earthquake), focal depth of the earthquake (FD), water depth at the source area (d_0), bathymetric features along the tsunami propagation path that may cause several natural interferences such as reflection of the waves, potential harbor resonance and edge waves (e.g. Raichlen and Lee, 1991; Synolakis, 2003; Yalciner, and Pelinovsky, 2007; Heidarzadeh et al., 2009; Shimozono et al., 2012; Saito et al., 2014). Precise analysis of these effects normally requires numerous numerical simulations which is beyond the scope of this study.

Here, we focus on two of the above-mentioned factors: water depth at the source region and earthquake focal depth. The effect of water depth at the source region (d_0) on the coastal amplitude of a tsunami (η) can be explained by Green's law (Sorensen, 2010):

$$\eta = \eta_0 \left(\frac{d_0}{d}\right)^{1/4} \tag{2}$$

where, d is water depth at the coast and η_0 is amplitude of coseismic crustal deformation. By assuming constant water depth at the coast (d),

Equation (2) indicates that the deeper the water depth at the source area (d_0), the larger the coastal amplitude of a tsunami (η) would be. Regarding earthquake focal depth (FD), it is widely known that deeper earthquakes generate smaller tsunamis and vice versa (e.g. Synolakis, 2003; Satake, 2014).

To quantitatively study the effects of earthquake focal depth (FD) and water depth at the source region (d_0) on coastal amplitude of tsunamis, we compare these two parameters for five M_w7.8 thrust events (Fig. 9). These events and the respective references are: 2006 Java (Fujii and Satake, 2006), 2012 Haida Gwaii (Gusman et al., 2016; Leonard and Bednarski, 2014), 2016 Kaikoura (Power et al., 2017; Heidarzadeh and Satake, 2017) and 2016 Ecuador (Heidarzadeh et al., 2017b). Fig. 9 indicates that for similar-size and similar-mechanism earthquakes, coastal tsunami height (or runup) is directly correlated with d_0 (Fig. 9b), but is inversely related to focal depth (FD) (Fig. 9c). Therefore, the small coastal amplitude of the 2020 Alaska tsunami can be explained by the relatively deep focal depth of the earthquake (FD = 28 km) and the extremely shallow water depth around the source region (d_0 = 100–200 m).

7. Conclusions

The tsunami generated by July 2020 M_w7.8 thrust earthquake was unusual in two ways: (i) the period of the tsunami was very long (51–64 min) and (ii) its coastal amplitude was small (~0.5 m). This study was motivated to explain these peculiar characteristics of the 2020 tsunami. Here, we applied waveform analysis and numerical simulations and achieved the following conclusions:

● The deep-ocean zero-to-crest amplitude of the tsunami was 0.3–1.0 cm (average = 0.6 cm) whereas the coastal amplitude recorded on tide gauges was 5.7–24.0 cm (average = 14.9 cm). Tsunami period from this M_w7.8 earthquake was 51–64 min which is much longer than that generated by the 2011 M_w9.0 Japan earthquake (20–26 min).

● We proposed a source model for this tsunami comprising length and width of 110 km and 70 km, respectively, with uniform slip of 1.7 m. This source model is located at the water depth of 100–200 m. Our model successfully reproduces the observed tsunami waveforms.

● By applying a simple analytical equation for the period of tsunami waves, we showed that the ultra-long period of the 2020 Alaska tsunami (51–64 min) can be reproduced using the water depth around the source region (100–200 m) and the length of the coseismic deformation area (~100 km).

● Comparison of the coastal amplitude of the 2020 Alaska event (~0.5 m) with four other similar-size and similar-mechanism earthquakes revealed that the smaller coastal amplitude of this tsunami is due to
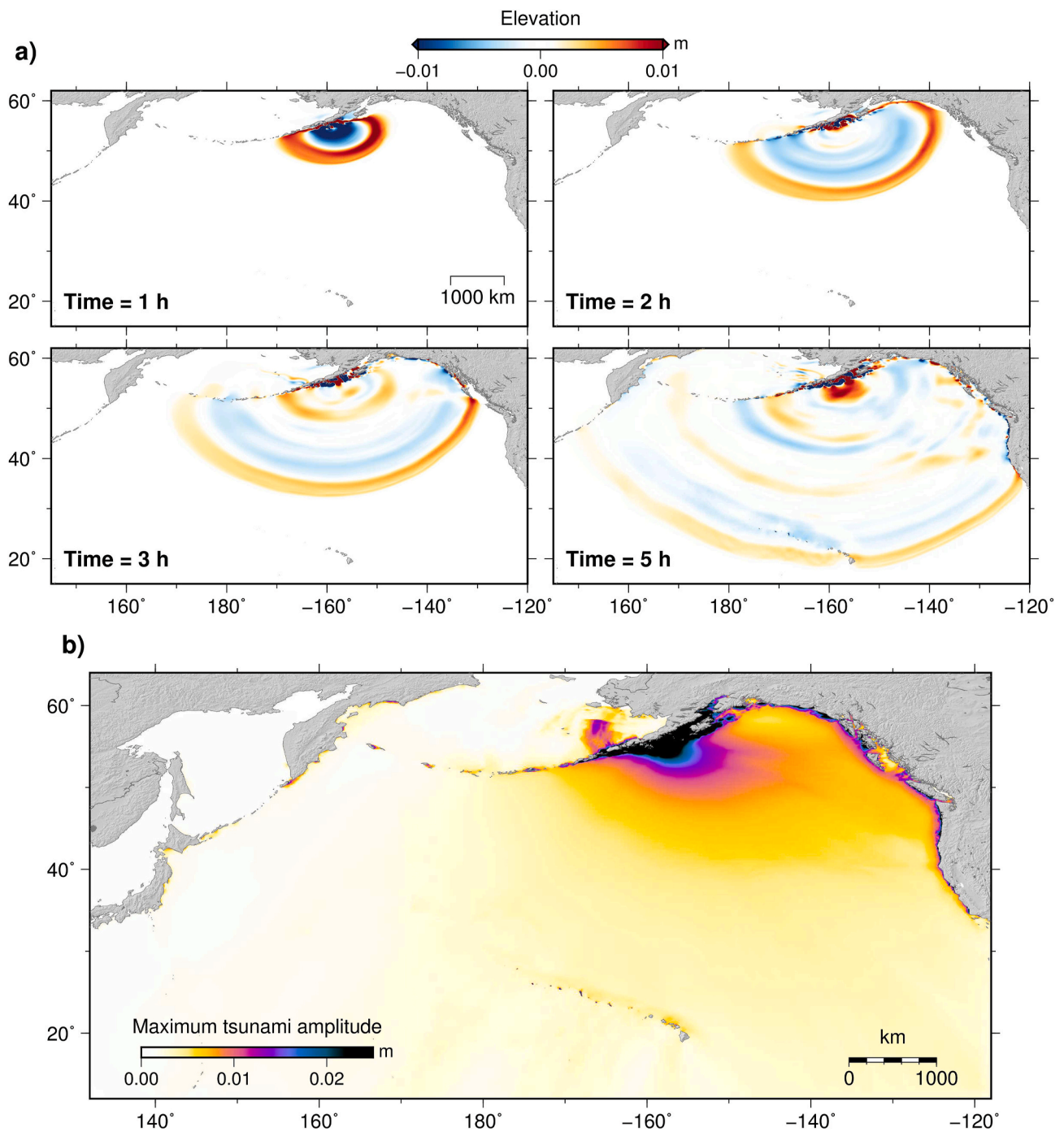
Fig. 6. a. Tsunami propagation snapshots at times 1 h, 2 h, 3 h and 5 h for the July 22, 2020 Alaska (USA) tsunami. **b.** Maximum tsunami amplitudes during the entire tsunami simulation time.
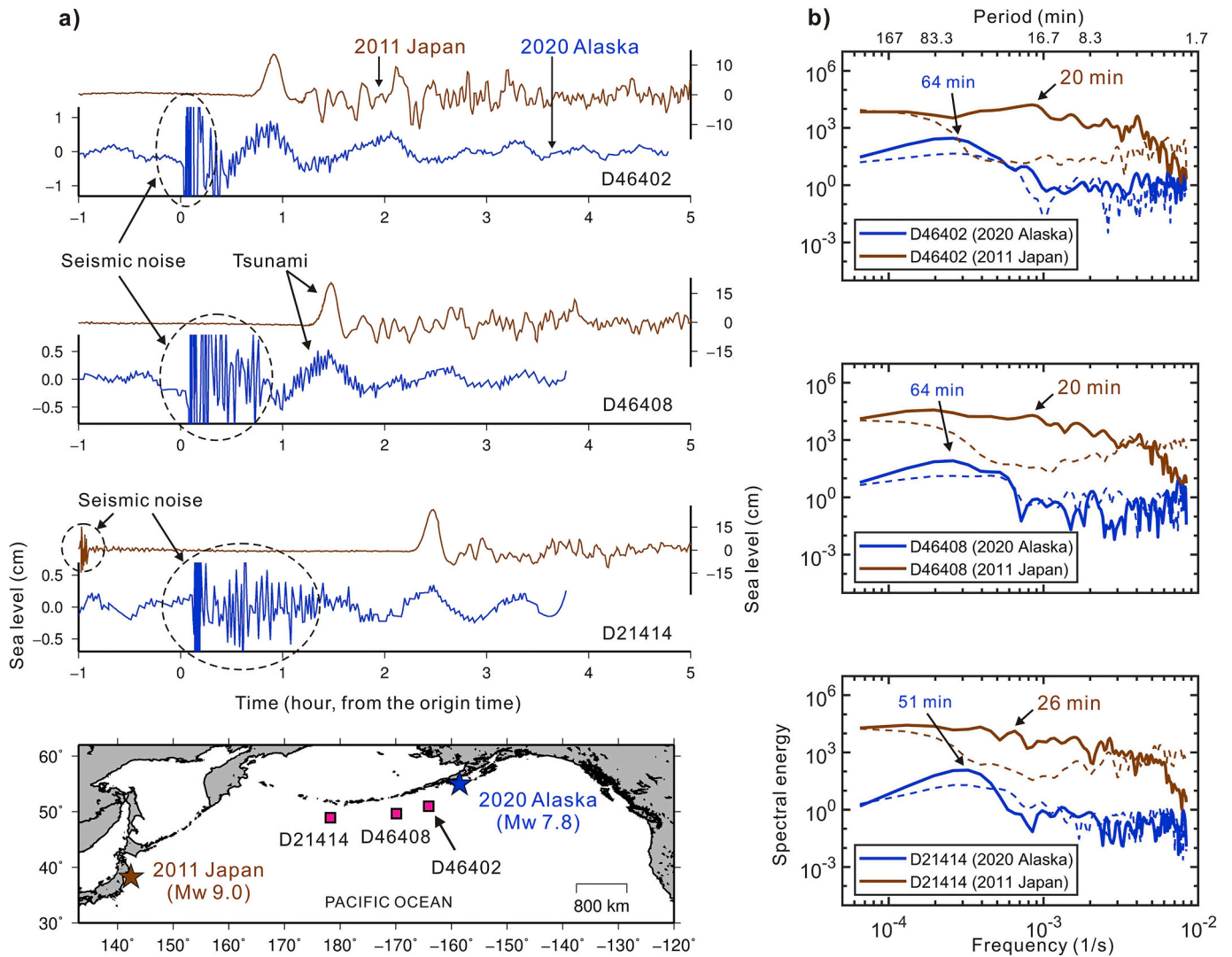
Fig. 7. a. Comparison of the observed DART waveforms of the 2020 Alaska tsunami (blue) with those of the 2011 Japan tsunami (brown). The 2011 Japan tsunami waveforms are shifted in time to align with the first peak of the 2020 Alaska tsunami waveforms. **b.** Respective spectra for each DART tsunami waveform (solid lines). The dashed lines are spectra for the background signals before tsunami arrivals at each station. (For interpretation of the references to color in this figure legend, the reader is referred to the Web version of this article.)
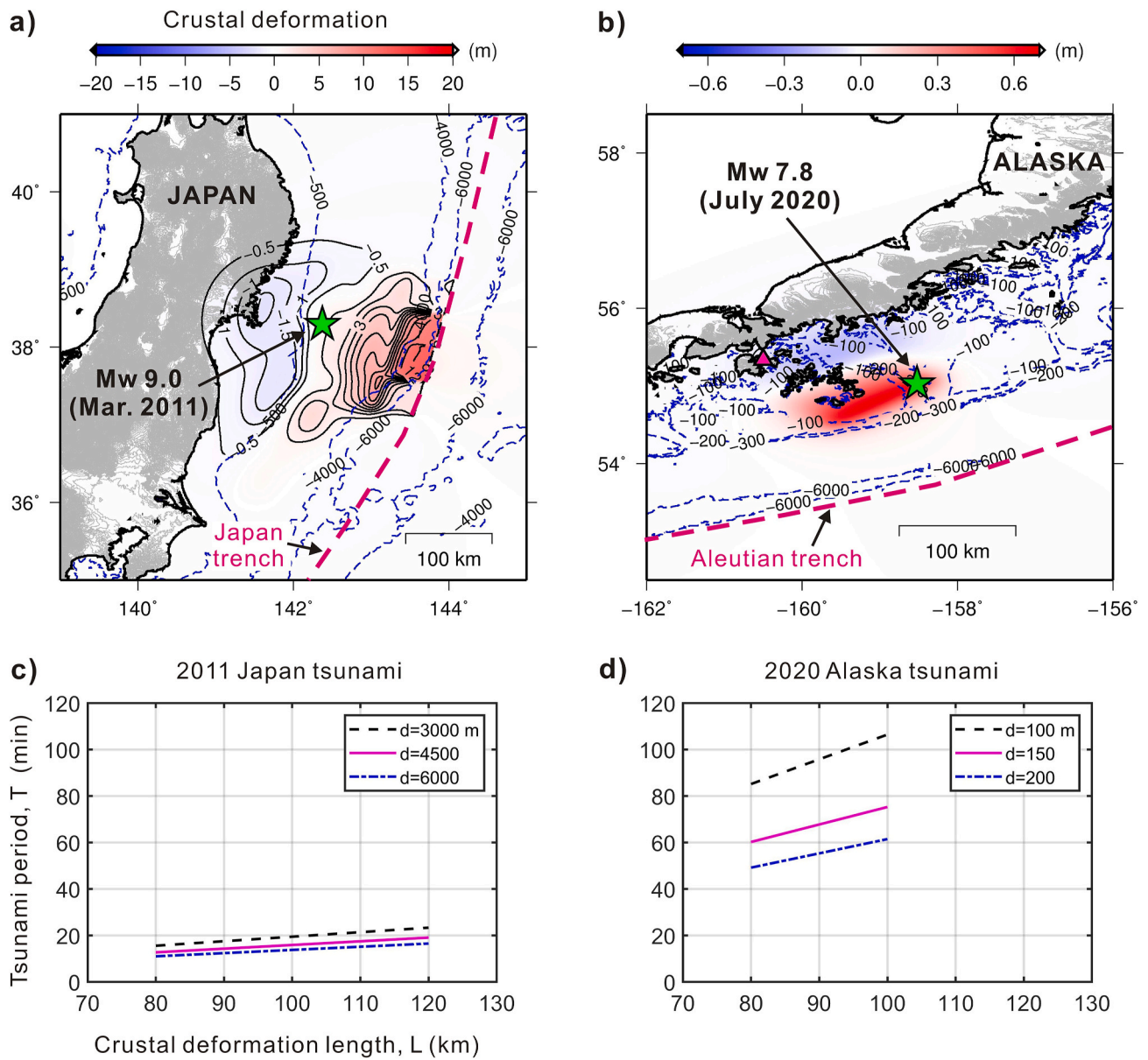
Fig. 8. a. Crustal deformation due to the 2011 Japan earthquake (M_w9.0) based on the source model by Fujii et al. (2011). **b.** Crustal deformation due to the recent July 2020 Alaska earthquake (M_w7.8) based on our uniform-fault model. **c.** Theoretical values of tsunami period for the 2011 Japan tsunami based Equation (1) and using the water depth at the tsunami source (d = 3000 m, 4500 m, 6000 m) as well as crustal deformation length. **d.** Same as panel "c" but for the 2020 Alaska tsunami.
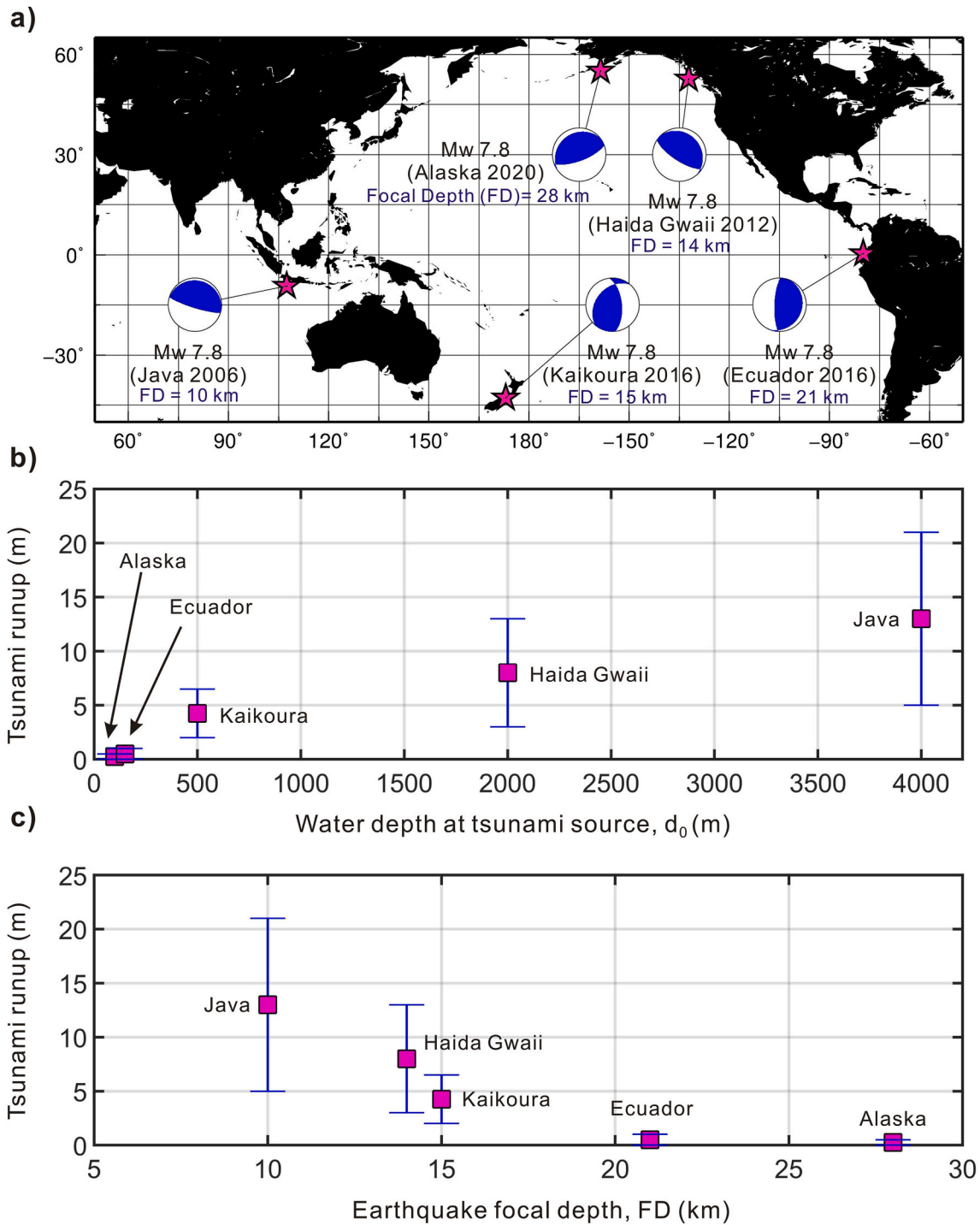
Fig. 9. a. Epicenters (stars) and focal mechanisms (blue/white circles) of a few $M_w7.8$ thrust earthquakes worldwide. **b.** Variations of tsunami runups and water depths at the tsunami sources for events shown in panel "a". Vertical blue bars give the ranges of tsunami runups for each event while pink squares are the average values. **c.** Same as panel "b" but for earthquake focal depth (FD). (For interpretation of the references to color in this figure legend, the reader is referred to the Web version of this article.)

the relatively deep focal depth of the earthquake (28 km) and the extremely shallow water around the source region (100–200 m).

Credit author statement

The lead author, Mohammad Heidarzadeh, initiated the research and conceptualized and organized all activities reported in this article. Waveform analyses, spectral analyses and wavelet analyses are

conducted by Mohammad Heidarzadeh. The second author, Iyan E. Mulia, conducted numerical simulations of the tsunami.

Declaration of competing interest

The authors declare that they have no known competing financial interests or personal relationships that could have appeared to influence the work reported in this paper.

Acknowledgements

References

An, C., Cai, C., Zheng, Y., Meng, L., Liu, P., 2017. Theoretical solution and applications of ocean bottom pressure induced by seismic seafloor motion. Geophys. Res. Lett. 44 (20), 10–272.

An, C., Liu, H., Ren, Z., Yuan, Y., 2018. Prediction of tsunami waves by uniform slip models. J. Geophys. Res. 123 (11), 8366–8382.

Baba, T., Takahashi, N., Kaneda, Y., Ando, K., Matsuoka, D., Kato, T., 2015. Parallel implementation of dispersive tsunami wave modeling with a nesting algorithm for the 2011 Tohoku tsunami. Pure Appl. Geophys. 172 (12), 3455–3472.

Ben-Menahem, A., Rosenman, M., 1972. Amplitude patterns of tsunami waves from submarine earthquakes. J. Geophys. Res. 77 (17), 3097–3128.

Clague, J.J., Bobrowsky, P.T., Hamilton, T.S., 1994. A sand sheet deposited by the 1964 Alaska tsunami at Port Alberni, British Columbia. Estuar. Coast Shelf Sci. 38 (4), 413–421.

Courant, R., Friedrichs, K., Lewy, H., 1928. Über die partiellen Differenzengleichungen der mathematischen Physik. Math. Ann. 100 (1), 32–74.

Fujii, Y., Satake, K., 2006. Source of the July 2006 West Java tsunami estimated from tide gauge records. Geophys. Res. Lett. 33 (24).

Fujii, Y., Satake, K., Sakai, S.I., Shinohara, M., Kanazawa, T., 2011. Tsunami source of the 2011 off the pacific coast of tohoku earthquake. Earth Planets Space 63 (7), 55.

Geoware, 2011. The Tsunami Travel Times (TTT) Package. http://www.geoware-online.com/tsunami.html.

Grinsted, A., 2008. Tidal Fitting Toolbox. https://uk.mathworks.com/matlabcentral/fileexchange/19099-tidal-fitting-toolbox?focused=3854016&tab=function&s_tid=gn_loc_drop. (Accessed 19 May 2020).

Gusman, A.R., Murotani, S., Satake, K., Heidarzadeh, M., Gunawan, E., Watada, S., Schurr, B., 2015. Fault slip distribution of the 2014 Iquique, Chile, earthquake estimated from ocean-wide tsunami waveforms and GPS data. Geophys. Res. Lett. 42 (4), 1053–1060.

Gusman, A.R., Sheehan, A.F., Satake, K., Heidarzadeh, M., Mulia, I.E., Maeda, T., 2016. Tsunami data assimilation of Cascadia seafloor pressure gauge records from the 2012 Haida Gwaii earthquake. Geophys. Res. Lett. 43 (9), 4189–4196.

Haeussler, P.J., Parsons, T., Finlayson, D.P., Hart, P., Chaytor, J.D., Ryan, H., Lee, H., Labay, K., Peterson, A., Liberty, L., 2014. New imaging of submarine landslides from the 1964 earthquake near Whittier, Alaska, and a comparison to failures in other Alaskan fjords. Submarine Mass Movements and Their Consequences. Springer, Cham, pp. 361–370.

Heidarzadeh, M., Satake, K., 2015. New insights into the source of the Makran Tsunami of 27 November 1945 from Tsunami waveforms and coastal deformation data. Pure Appl. Geophys. 172 (3), 621–640.

Heidarzadeh, M., Satake, K., 2017. Possible dual earthquake–landslide source of the 13 November 2016 Kaikoura, New Zealand tsunami. Pure Appl. Geophys. 174 (10), 3737–3749. https://doi.org/10.1007/s00024-017-1637-4.

Heidarzadeh, M., Pirooz, M.D., Zaker, N.H., Yalciner, A.C., 2009. Modeling the near-field effects of the worst possible tsunami in the Makran subduction zone. Ocean. Eng. 36 (5), 368–376.

Heidarzadeh, M., Necmioglu, O., Ishibe, T., Yalciner, A.C., 2017a. Bodrum-Kos (Turkey-Greece) Mw 6.6 earthquake and tsunami of 20 July 2017: a test for the Mediterranean tsunami warning system. Geoscience Lett 4, 31. https://doi.org/10.1186/s40562-017-0097-0.

Heidarzadeh, M., Murotani, S., Satake, K., Takagawa, T., Saito, T., 2017b. Fault size and depth extent of the Ecuador earthquake (Mw 7.8) of 16 April 2016 from teleseismic and tsunami data. Geophys. Res. Lett. 44 (5), 2211–2219.

Heidarzadeh, M., Tappin, D.R., Ishibe, T., 2019. Modeling the large runup along a narrow segment of the Kaikoura coast, New Zealand following the November 2016 tsunami from a potential landslide. Ocean. Eng. 175, 113–121. https://doi.org/10.1016/j.oceaneng.2019.02.024.

Heidarzadeh, M., Ishibe, T., Sandanbata, O., Muhari, A., Wijanarto, A.B., 2020. Numerical modeling of the subaerial landslide source of the 22 December 2018 Anak Krakatoa volcanic tsunami, Indonesia. Ocean. Eng. 195 https://doi.org/10.1016/j.oceaneng.2019.106733.

Ioc, I.H.O., BODC, 2003. Centenary Edition of the GEBCO Digital Atlas, Published on CD-ROM on Behalf of the Intergovernmental Oceanographic Commission and the International Hydrographic Organization as Part of the General Bathymetric Chart of the Oceans. British Oceanographic Data Centre, Liverpool.

Johnson, J.M., Satake, K., 1997. Estimation of seismic moment and slip distribution of the April 1, 1946, Aleutian tsunami earthquake. J. Geophys. Res. 102 (B6), 11765–11774.

Leonard, L.J., Bednarski, J.M., 2014. Field survey following the 28 October 2012 Haida Gwaii tsunami. Pure Appl. Geophys. 171 (12), 3467–3482.

Li, S., Freymueller, J., McCaffrey, R., 2016. Slow slip events and time-dependent variations in locking beneath Lower Cook Inlet of the Alaska-Aleutian subduction zone. J. Geophys. Res. 121 (2), 1060–1079.

López, A.M., Okal, E.A., 2006. A seismological reassessment of the source of the 1946 Aleutian 'tsunami' earthquake. Geophys. J. Int. 165 (3), 835–849.

Mathworks, 2020. MATLAB User Manual. MathWorks Inc., MA, USA, p. 282.

Okada, Y., 1985. Surface deformation due to shear and tensile faults in a half-space. Bull. Seismol. Soc. Am. 75, 1135–1154.

Okal, E.A., 1988. Seismic parameters controlling far-field tsunami amplitudes: a review. Nat. Hazards 1 (1), 67–96.

Okal, E.A., Synolakis, C.E., Fryer, G.J., Heinrich, P., Borrero, J.C., Ruscher, C., Arcas, D., Guille, G., Rousseau, D., 2002. A field survey of the 1946 Aleutian tsunami in the far field. Seismol Res. Lett. 73 (4), 490–503.

Plafker, G., Kachadoorian, R., Eckel, E.B., Mayo, L.R., 1969. Effects of the earthquake of March 27, 1964 on various communities. Geological Survey Professional Paper 542-G. US Government Printing Office, Washington DC, p. 61.

Power, W., Clark, K., King, D.N., Borrero, J., Howarth, J., Lane, E.M., et al., 2017. Tsunami runup and tide-gauge observations from the 14 November 2016 M7.8 Kaikoura earthquake, New Zealand. Pure Appl. Geophys. 174, 2457–2473. https://doi.org/10.1007/s00024-017-1566-2.

Rabinovich, A.B., 1997. Spectral analysis of tsunami waves: separation of source and topography effects. J. Geophys. Res. 102 (C6), 12663–12676.

Raichlen, F., Lee, J., 1991. Oscillation of bays, harbors, and lakes. In: Herbich, J. (Ed.), Handbook of Coastal and Ocean Engineering. Gulf Publishing Co, Houston.

Saito, T., Inazu, D., Miyoshi, T., Hino, R., 2014. Dispersion and nonlinear effects in the 2011 Tohoku-Oki earthquake tsunami. J. Geophys. Res. 119 (8), 5160–5180.

Sallarès, V., Ranero, C.R., 2019. Upper-plate rigidity determines depth-varying rupture behaviour of megathrust earthquakes. Nature 576 (7785), 96–101.

Satake, K., 1987. Inversion of tsunami waveforms for the estimation of a fault heterogeneity: method and numerical experiments. J. Phys. Earth 35 (3), 241–254.

Satake, K., 2014. Advances in earthquake and tsunami sciences and disaster risk reduction since the 2004 Indian ocean tsunami. Geoscience Lett 1 (1), 15.

Satake, K., Heidarzadeh, M., 2017. A review of source models of the 2015 Illapel, Chile earthquake and insights from tsunami data. Pure Appl. Geophys. 174 (1), 1–9.

Satake, K., Heidarzadeh, M., Quiroz, M., Cienfuegos, R., 2020. History and features of trans-oceanic tsunamis and implications for paleo-tsunami studies. Earth Sci. Rev. 202 https://doi.org/10.1016/j.earscirev.2020.103112.

Shimozono, T., Sato, S., Okayasu, A., Tajima, Y., Fritz, H.M., Liu, H., Takagawa, T., 2012. Propagation and inundation characteristics of the 2011 Tohoku tsunami on the central Sanriku coast. Coast Eng. J. 54, 1250004, 01.

Sorensen, R.M., 2010. Basic Coastal Engineering, third ed. Springer Science & Business Media, p. 324.

Stauder, W., Bollinger, G.A., 1966. The focal mechanism of the Alaska earthquake of March 28, 1964, and of its aftershock sequence. J. Geophys. Res. 71 (22), 5283–5296.

Synolakis, C.E., 2003. Tsunami and seiche. In: Chen, W.F., Scawthorn, C. (Eds.), Earthquake Engineering Handbook. CRC Press, Boca Raton, FL, pp. 1–90 (Chapter 9).

Synolakis, C.E., Bernard, E.N., 2006. Tsunami science before and beyond boxing day 2004. Phil. Trans. R. Soc. A 364 (1845), 2231–2265.

Torrence, C., Compo, G., 1998. A practical guide to wavelet analysis. Bull. Am. Meteorol. Soc. 79, 61–78.

Weatherall, P., Marks, K.M., Jakobsson, M., et al., 2015. A new digital bathymetric model of the world's oceans. Earth Space Sci 2, 331–345.

Welch, P., 1967. The use of fast Fourier transform for the estimation of power spectra: a method based on time averaging over short, modified periodograms. IEEE Transactions Audio Electroacoustics AE- 15, 70–73.

Wessel, P., Smith, W.H.F., 1998. New, improved version of generic mapping tools released. EOS Trans. AGU 79 (47), 579.

Yalciner, A.C., Pelinovsky, E.N., 2007. A short cut numerical method for determination of periods of free oscillations for basins with irregular geometry and bathymetry. Ocean. Eng. 34 (5–6), 747–757.

Yokota, Y., Koketsu, K., Fujii, Y., Satake, K., Sakai, S.I., Shinohara, M., Kanazawa, T., 2011. Joint inversion of strong motion, teleseismic, geodetic, and tsunami datasets for the rupture process of the 2011 Tohoku earthquake. Geophys. Res. Lett. 38 (7) https://doi.org/10.1029/2011GL050098.